ACS APPLIED MATERIALS & INTERFACES

Research Article

www.acsami.org

High-Performance Asymmetric Supercapacitor Based on Graphene Hydrogel and Nanostructured MnO_2

Hongcai Gao, Fei Xiao, Chi Bun Ching, and Hongwei Duan*

School of Chemical and Biomedical Engineering, Nanyang Technological University, 70 Nanyang Drive, Singapore 637457

Supporting Information

ABSTRACT: We have successfully fabricated an asymmetric supercapacitor with high energy and power densities using graphene hydrogel (GH) with 3D interconnected pores as the negative electrode and vertically aligned MnO_2 nanoplates on nickel foam (MnO_2-NF) as the positive electrode in a neutral aqueous Na_2SO_4 electrolyte. Because of the desirable porous structure, high specific capacitance and rate capability of GH and MnO_2-NF, complementary potential window of the two electrodes, and the elimination of polymer binders and conducting additives, the asymmetric supercapacitor can be cycled reversibly in a wide potential window of 0−2.0 V and exhibits an energy density of 23.2 Wh kg^{-1} with a power density of 1.0 kW kg^{-1}. Energy density of the asymmetric supercapacitor is significantly improved in comparison with those of symmetric supercapacitors based on GH (5.5 Wh kg^{-1}) and MnO_2-NF (6.7 Wh kg^{-1}). Even at a high power density of 10.0 kW kg^{-1}, the asymmetric supercapacitor can deliver a high energy density of 14.9 Wh kg^{-1}. The asymmetric supercapacitor also presents stable cycling performance with 83.4% capacitance retention after 5000 cycles.

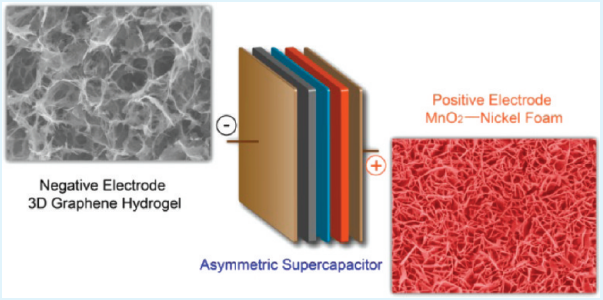

KEYWORDS: *graphene hydrogel, manganese oxide nanoplates, cathodic electrodeposition, asymmetric supercapacitor, energy storage*

1. INTRODUCTION

Supercapacitors represent an emerging class of energy storage devices that have attracted increasing attention because of a number of important features including high power density, fast charging/discharging rate, and excellent cycle stability.[1−3] Such outstanding properties make them promising in a wide range of applications from hybrid vehicles and portable electronics to military devices, where high power density and long cycle-life are highly desirable. However, the low energy density (normally less than 10 Wh kg^{-1}) of commercially available supercapacitors has imposed significant challenges in employing them as primary power sources to replace batteries.[4] Recently, concentrated efforts have been made to tackle this problem by developing nanostructured electrode materials with improved specific capacitance and increasing the operating voltage of a supercapacitor.[5−7] In particular, two strategies are commonly explored for the design of high-voltage supercapacitors, i.e., replacing aqueous electrolytes with organic electrolytes[8,9] or ionic liquids[10,11] having wider potential windows and developing hybrid (asymmetric) supercapacitors with both capacitive electrode as power source and Faradic electrode as energy source.[12−14] However, nonaqueous electrolytes typically suffer from limited ionic conductivity and also raise safety concerns about the potential environmental impact in case of leakage. On the other hand, the construction of asymmetric supercapacitors is an effective approach to extend the cell potential window of aqueous electrolytes beyond the thermodynamic limit of ~1.2 V and thus significantly improve the energy density.[15−18] The combination of appropriate electrode materials working in well-separated potential windows in the same electrolyte is essential to achieve high energy density and power density of asymmetric supercapacitors.[19−21]

In this Article, we reported a new design of asymmetric supercapacitor based on graphene hydrogel (GH) with 3D interconnected pores and a hierarchical composite of vertically aligned MnO_2 nanoplates on nickel foam (MnO_2-NF) as negative and positive electrodes, respectively (Scheme 1). Carbon materials, exhibiting complementary electrochemical windows to various pseudocapacitive materials of transition metal oxides and conducting polymers, are most widely used as negative electrodes in asymmetric supercapacitors.[22,23] Graphene consisting of hexagonally bonded sp^2 carbon atoms is actively investigated for supercapacitor applications due to its high specific surface area, excellent electrical conductivity and chemical stability.[24,25] However, the aggregation and restacking of graphene nanosheets during processing leads to significantly reduced surface areas and therefore becomes a serious obstacle to take the full advantage of the structural characteristics of graphene. Our results have shown that assembling graphene nanosheets into GH with a 3D network structure during the chemical reduction of graphene oxides (GO) can effectively prevent the aggregation of graphene nanosheets. Consequently, GH as electrode materials provides large active surface areas,

Received: March 13, 2012
Accepted: April 30, 2012
Published: April 30, 2012

 © 2012 American Chemical Society

Scheme 1. Schematic Illustration of the Fabrication Process of an Asymmetric Supercapacitor Based on GH as the Negative Electrode and MnO_2-NF as the Positive Electrode

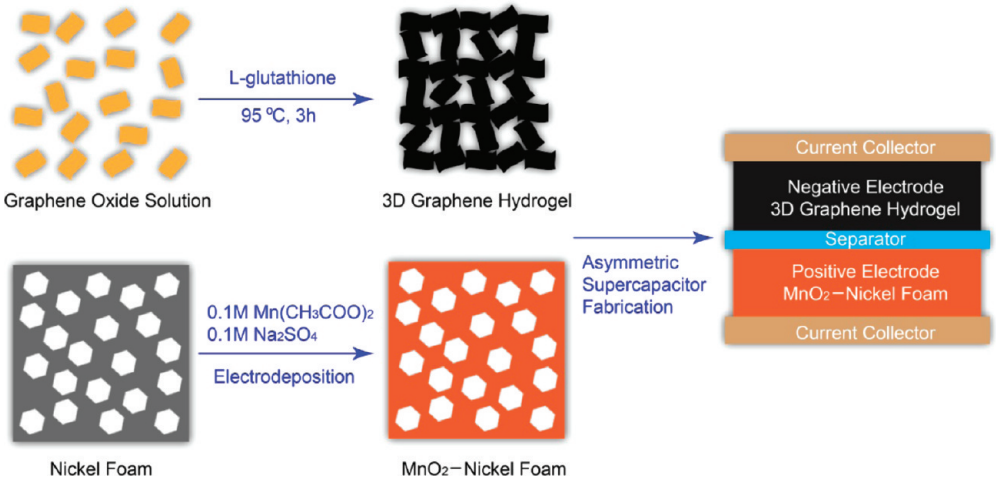

facilitates electrolyte ion transportation, and demonstrates an enhanced energy storage capacity and a good rate capability. One interesting finding is that an eco-friendly reagent of L-glutathione allows for one to produce robust GH from GO dispersion under mild conditions, offering greater flexibility than the time-consuming hydrothermal method previously reported.[26,27]

MnO_2 with pseudocapacitance is a highly attractive positive electrode material, benefiting from its low cost, abundance, and remarkable electrochemical performance in aqueous electrolytes.[28−30] Varieties of wet-chemical and electrochemical methods have been developed to prepare nanostructured MnO_2.[31] Structural parameters, such as crystal type, morphology, and porosity, are the vital factors determining the electrochemical performance of MnO_2-based electrodes.[32] In this work, a hierarchical composite of MnO_2-NF was prepared by electrodeposition of MnO_2 nanoplates on highly conductive porous nickel foam through cathodic electrodeposition and directly used as electrodes for supercapacitors without further processing. Importantly, the porous structure of nickel foam allows a higher mass loading of active materials per area, facilitates the electrolyte ion transportation and reaction with the active materials, and eventually leads to improved utilization efficiency of active materials. Compared with anodic deposition in which a positive potential is applied to oxidize starting Mn^{2+} into Mn^{4+} and deposit as MnO_2,[33,34] cathodic deposition of MnO_2 can avoid the oxidation and dissolution of low-cost metallic current collectors.[35,36] Moreover, a robust contact endowed by electrodeposition is formed between MnO_2 nanostructures and the highly conductive nickel foam, which can cope with the problems of poor electrical conductivity and rate capability of MnO_2 when used as electrode materials. Collectively, taking advantages of GH with 3D interconnected pores, vertically aligned MnO_2 nanoplates with sufficient free spaces, and robust contact between MnO_2 and nickel foam, we have found that the fabricated asymmetric supercapacitor of GH//MnO_2-NF can be cycled reversibly in a wide potential window of 0−2.0 V and exhibits a much higher energy density of 23.2 Wh kg^{-1} than that of the symmetric supercapacitors of GH//GH (5.5 Wh kg^{-1}) and MnO_2-NF//MnO_2-NF (6.7 Wh kg^{-1}) at a current density of 1 A g^{-1}. Furthermore, the asymmetric supercapacitor displays remarkable cycling stability with capacitance retention of 83.4% after 5000 continuous charge/discharge cycles.

2. EXPERIMENTAL SECTION

2.1. Preparation of Samples. GO were synthesized from graphite powder (Sigma-Aldrich) according to the modified Hummers' method.[37,38] GH was prepared by the following procedure using L-glutathione as the reducing agent. Briefly, GO aqueous dispersion (2.0 mg mL^{-1}) was loaded in a glass vial. Then, L-glutathione was added to get a concentration of 4.0 mg mL^{-1}. After stirring for 60 min to dissolve the L-glutathione, the as-prepared dispersion was heated at 95 °C for 3 h without any disturbance to produce GH. The dispersion of reduced GO (RGO) was also prepared using L-glutathione as a reducing agent at the same temperature under continuous stirring. After the chemical reduction, the excess L-glutathione was removed by dialysis.

MnO_2-NF was prepared by electrodeposition of MnO_2 on nickel foam (1 cm × 1 cm) which was first cleaned by ethanol and deionized water. Platinum wire and saturated calomel electrode (SCE) were used as the counter and reference electrodes, respectively. The cathodic electrodeposition of MnO_2 nanoplate arrays was carried out in aqueous solution containing 0.1 M manganese acetate and 0.1 M sodium sulfate according to a method previously reported with some modification.[39] The electrodeposition of MnO_2 on nickel foam was carried out at a constant potential of −1.6 V for different periods of time from 50 to 200 s to control the amount of the MnO_2 deposited. After deposition, the nickel foam was rinsed in deionized water for several times and then dried at ambient temperature. The accurate weight of electrodeposited MnO_2 was determined by a high-precision balance with sensitivity of 0.01 mg (Denver Instrument).

The obtained GH cylinder was freeze-dried, cut into pieces, and directly used as electrode to fabricate symmetric supercapacitor of GH//GH. MnO_2-NF was also directly used to fabricate symmetric supercapacitor of MnO_2-NF//MnO_2-NF. To construct the asymmetric supercapacitor of GH//MnO_2-NF, the loading mass ratio of active materials (GH:MnO_2) was estimated to be 1.2 according to the specific capacitance calculated from their symmetric supercapacitors, and each electrode contained about 1.0 mg of active material. The two electrodes were separated by a glass-fiber separator and assembled in a Swagelok-type cell. Aqueous Na_2SO_4 solution (0.5 M) was used as the electrolyte. The specific capacitance of a supercapacitor cell (C_t) was calculated using the equations $C_t = I\Delta t/m\Delta V$, where I is the constant discharge current, Δt is the discharging time, m is the total mass of active materials in both electrodes, and ΔV is the voltage drop upon discharging (excluding IR drop). In symmetric supercapacitors, the specific capacitance (C_{sc}) of the electrode (GH or MnO_2-NF) was calculated following the equations $C_{sc} = 4C_t$. The energy density (E)

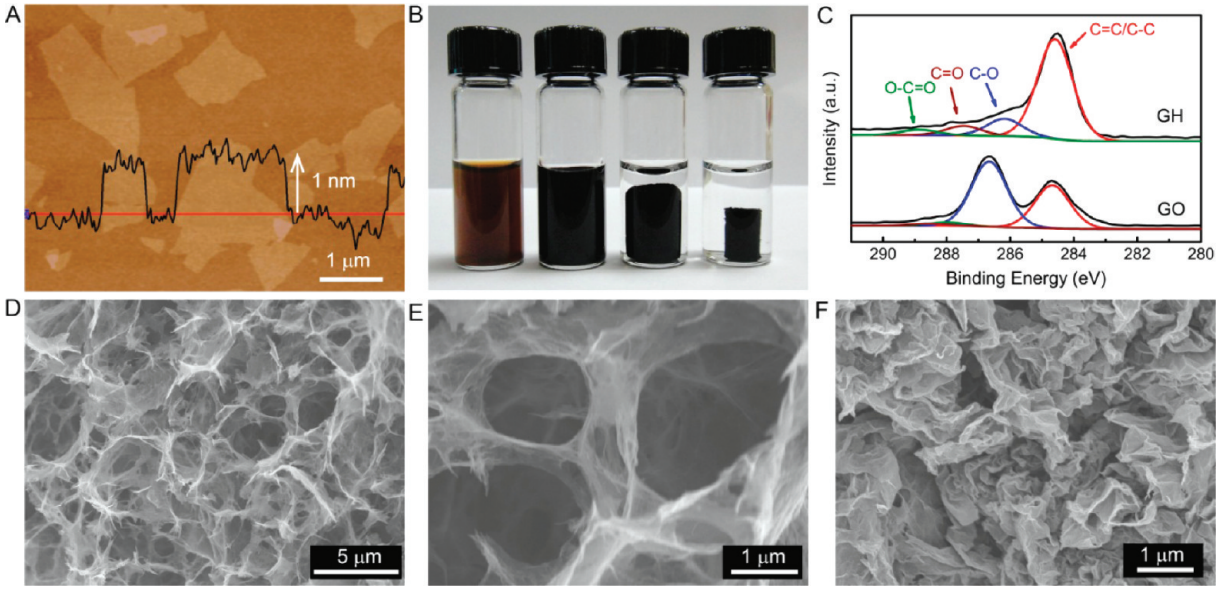

Figure 1. (A) AFM images of GO dispersion spin-coated on silicon wafer. (B) Photograph of aqueous mixture of GO and L-glutathione at different reaction times of 0, 30, 60, and 180 min (from left to right). (C) High resolution XPS spectra of C 1s for GO and GH. (D and E) SEM images of freeze-dried GH at low and high magnification. (F) SEM images of freeze-dried RGO.

and power density (P) of a supercapacitor cell in the Ragone plots were calculated using the equations of $E = C_t\Delta V^2/2$ and $P = E/\Delta t$, respectively.[40,41]

2.2. Materials Characterization. The microstructures of the materials were examined by field-emission scanning electron microscopy (SEM) (JSM-6701F, JEOL) and atomic force microscopy (AFM) (MFP3D microscope, Asylum Research). SEM was equipped to perform elemental analysis by energy dispersive X-ray spectroscopy (EDS). The AFM samples were prepared by spin-coating the GO dispersion on silicon wafer with a 300 nm SiO_2 top layer and characterized with a silicon cantilever operating in tapping mode. Fourier transform infrared (FT-IR) spectra were obtained on a Perkin-Elmer Spectrum One Spectrometer. Raman spectra were acquired with a micro-Raman spectrometer (Reinshaw Raman Scope RM3000) at room temperature in the backscattering configuration with wavelength of 633 nm (1.96 eV). X-ray diffraction (XRD) patterns were collected with a Bruker AXS D8 X-ray diffractometer equipped with monochromatized Cu Kα radiation (λ = 1.54056 Å, 40 kV, and 20 mA). X-ray photoelectron spectroscopy (XPS) was performed on a Kratos-Axis spectrometer with monochromatic Al Kα ($h\nu$ = 1486.71 eV) X-ray radiation (15 kV and 10 mA) and a hemispherical electron energy analyzer. All XPS spectra were corrected according to the C 1s line at 284.6 eV. Curve fitting and background subtraction were accomplished using Casa XPS software. Quantachrome Autosorb 6B system was used to characterize the specific surface areas and pore structures of the electrode materials using nitrogen sorption under 77.4 K. The specific surface areas and pore size distributions of the electrode materials were calculated by Brunauer–Emmett–Teller (BET) and Barrett–Joyner–Halenda (BJH) methods, respectively. Cyclic voltammetry (CV), galvanostatic charge/discharge, and electrochemical impedance testes of supercapacitors were carried out on a CHI 660D electrochemical workstation.

3. RESULTS AND DISCUSSION

3.1. Negative Electrode Materials. Homogenous GO solution, synthesized from graphite powder according to the modified Hummers' method, was deposited on silicon wafer by spin-coating for AFM observation. As shown in Figure 1A, GO nanosheets are flat with a typical thickness of about 1.0 nm, indicating the complete exfoliation of graphite oxide into single-layered GO nanosheets.[38] L-Glutathione, an efficient, low-cost,

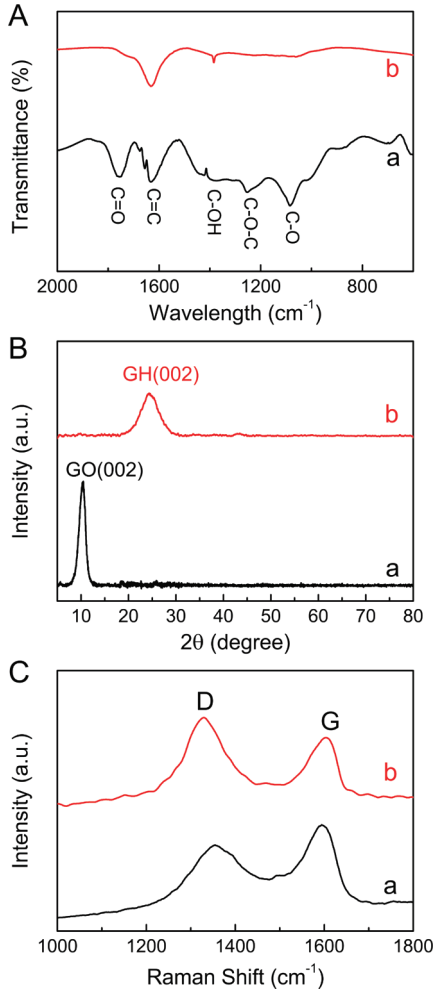

Figure 2. FT-IR spectra (A), XRD patterns (B), and Raman spectra (C) of GO (a) and GH (b).

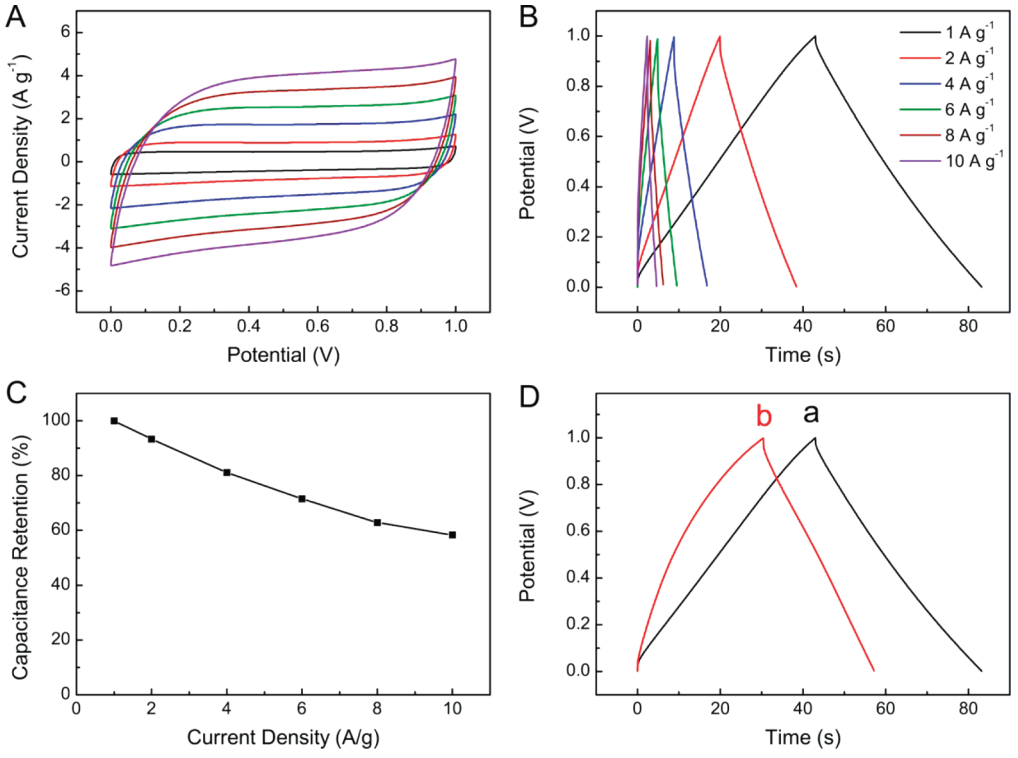

Figure 3. Electrochemical performance of the symmetric supercapacitor of GH//GH. (A) Cyclic voltammograms at different scan rates of 10, 20, 40, 60, 80, and 100 mV s^{-1} (from inner to outer). (B) Galvanostatic charge/discharge curves at different current densities of 1, 2, 4, 6, 8, and 10 A g^{-1}. (C) Capacitance retention ratio as a function of discharge current densities. (D) Galvanostatic charge/discharge curves of symmetric supercapacitors of GH//GH (a) and RGO//RGO (b) at current density of 1 A g^{-1}.

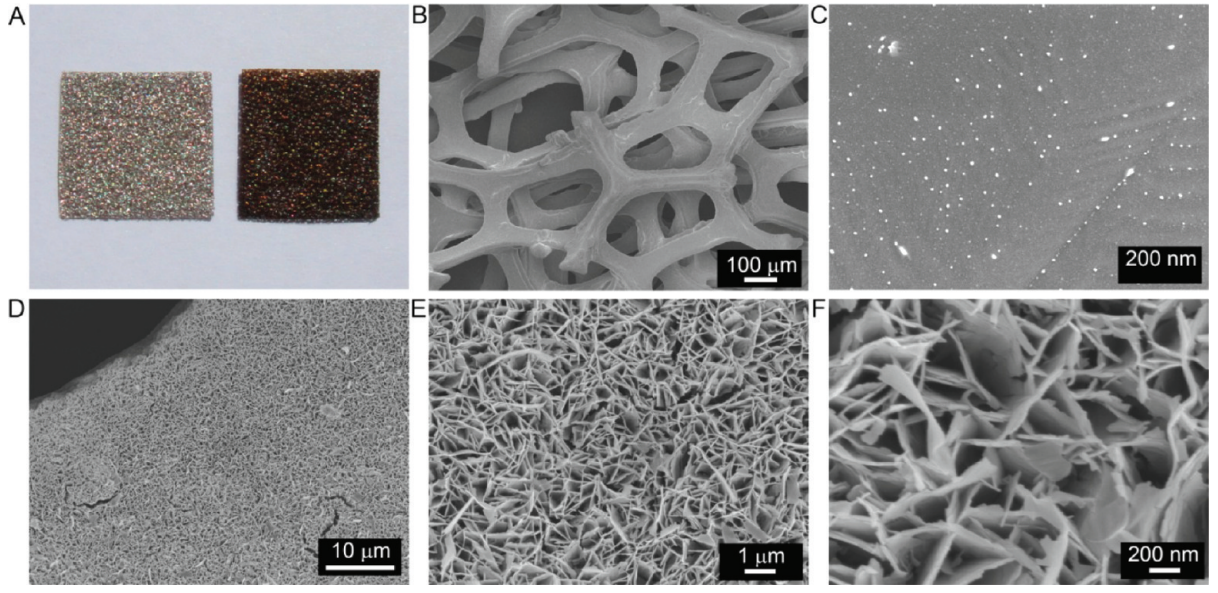

Figure 4. (A) Photographs of nickel foam before (left) and after (right) electrodeposition of MnO_2. (B and C) SEM images of bare nickel foam with low and high magnification. (D, E and F) SEM images of MnO_2 nanoplates electrodeposited on nickel foam at −1.6 V for 100 s with different magnifications.

and eco-friendly reducing agent, was selected for the chemical reduction of GO. Stable dispersion of graphene was obtained previously when a low concentration (0.1 mg mL^{-1}) of GO was reduced with L-glutathione under continuous stirring.[42] In this Article, we found that the use of concentrated GO dispersion (2.0 mg mL^{-1}) and the elimination of physical disturbance are essential for the self-assembly of graphene nanosheets into 3D structures of GH in this reaction system. A series of GO and L-glutathione dispersion was reacted at 95 °C for different time spans to investigate the gelation process (Figure 1B). Before the chemical reduction, GO was well dispersed in water forming a stable dark-brown colloidal suspension. After the addition of L-glutathione, gelation could not take place if the reaction time was less than 30 min. Further prolonging the

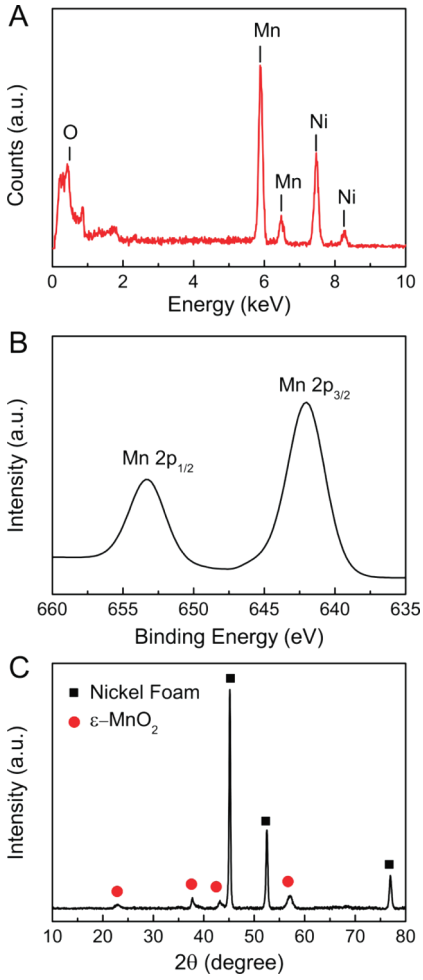

Figure 5. (A) EDS spectra of MnO_2-NF. (B) High resolution XPS spectra of MnO_2-NF for Mn $2p_{1/2}$ and Mn $2p_{3/2}$. (C) XRD pattern of MnO_2-NF.

reaction time to 60 min, a black cylinder of GH was obtained. After being treated for 180 min, the apparent size of the black cylinder decreased, and little change was observed subsequently.

The formation of 3D structured GH is attributed to the partial overlapping or coalescing of flexible reduced GO nanosheets via supramolecular interactions such as $\pi-\pi$ stacking and hydrogen bonding.[43,44] Reduction degree is also an important factor contributing to the formation of GH.[27] As the reduction proceeded, the graphene nanosheets assembled more tightly to form GH with 3D interconnected network structures (Figure S1, Supporting Information). The well-defined and interconnected 3D network of the resulting GH was revealed by typical SEM images (Figure 1D,E) of its freeze-dried sample. Plenty of pores with a wide size distribution are observed, and the solid walls of these pores are composed by randomly cross-linked and intertwisted graphene nanosheets. The BET specific surface areas of GH after reduction of 30, 60, and 180 min were measured to be 230.4, 259.8, and 315.2 m^2 g^{-1}, respectively (Figure S2, Supporting Information). Most pores of GH prepared at different times are in the mesoporous range with peaks centered at 2−10 nm. The increase of BET specific surface areas with the prolonged reaction time indicates the formation of 3D network of GH can effectively prevent the agglomeration and restacking of graphene sheets. The well-preserved 3D structure of GH can also greatly shorten the diffusion and migration paths of electrolyte ions during the rapid charge/discharge process. In addition, this unique 3D structure of GH enables the fabrication of self-supported supercapacitor electrodes, which is beneficial for improving the overall energy density of the supercapacitor by avoiding the utilization of conducting additives and polymer binders.[45] For comparison, a common strategy was employed to prepare the dispersion of reduced GO (RGO) using L-glutathione as a reducing agent but under continuous stirring. After filtration and freeze-drying, serious aggregation was observed due to the strong interactions between RGO nanosheets (Figure 1F), and the BET specific surface area of RGO is 210.9 m^2 g^{-1}, significantly smaller than that of GH (315.2 m^2 g^{-1}) (Figure S2, Supporting Information).

The successful reduction of GO by L-glutathione was confirmed by high resolution XPS spectra of C1s and FT-IR spectra. As shown in Figures 1C and 2A, the peaks of oxygen functionalities decreased significantly after the chemical reduction for 180 min, revealing that most of the oxygen functional groups on GO were removed. A two-step S_N2 nucleophilic reaction is the possible mechanism for the chemical reduction of GO by L-glutathione (Figure S3, Supporting Information).[46] The thiol group in L-glutathione is susceptible to oxidation and ready to release a proton, functioning as a nucleophile with high binding affinity to oxygen containing groups, such as hydroxyl and epoxide groups on GO to form water molecules.[47] Eventually, L-glutathione is oxidized into glutathione disulfide leading to the formation of RGO nanosheets. In the FT-IR spectra (Figure 2A), the characteristic stretching vibration peaks of C−S bonds in the range of 710−580 cm^{-1} were not detectable,[48] and no peaks from sulfur are observed in the EDS spectra of GH (Figure S4, Supporting Information). These results support the proposed reaction mechanism and also suggest the excess L-glutathione and glutathione disulfide were successfully removed by dialysis.

The structure of GO and GH was also studied by X-ray diffraction (XRD). According to the XRD patterns (Figure 2B), GO has a large interlayer distance of 0.85 nm (2θ = 10.3°) due to the presence of hydroxyl, epoxy, and carboxyl groups. After chemical reduction for 180 min, a broad peak centered at 2θ = 24.4° corresponding to an interlayer distance of 0.37 nm emerged, suggesting the poor ordering of graphene sheets along their stacking direction in GH.[49] The change of structure after the reduction process is further reflected in the Raman spectra of GO and GH (Figure 2C). Both of the spectra of GO and GH display the existence of D and G bonds located at 1352 and 1594 cm^{-1}. The intensity ratio (I_D/I_G) of D and G bands is 0.8 in GO and increases to 1.2 in GH, demonstrating that the chemical reduction altered the structure of GO and introduced a large number of structural defects.[50,51]

The electrical conductivity of GH was measured to be ~2 S m^{-1} based on a two-probe method.[26] This remarkable conductivity and its mechanical stability enable GH to be directly used as electrodes to fabricate supercapacitors without the need of polymer binder and conducting additives.[8] The performance of the symmetric supercapacitor of GH//GH was tested by cyclic voltammetry (CV) and galvanostatic charge/discharge in aqueous Na_2SO_4 electrolyte. The nearly rectangular CV curves manifest the ideal capacitive behavior of the supercapacitor (Figure 3A). Even at a high scan rate of 100 mV s^{-1}, the shapes of CV curves remain undistorted, implying low contact resistance in the supercapacitor. The

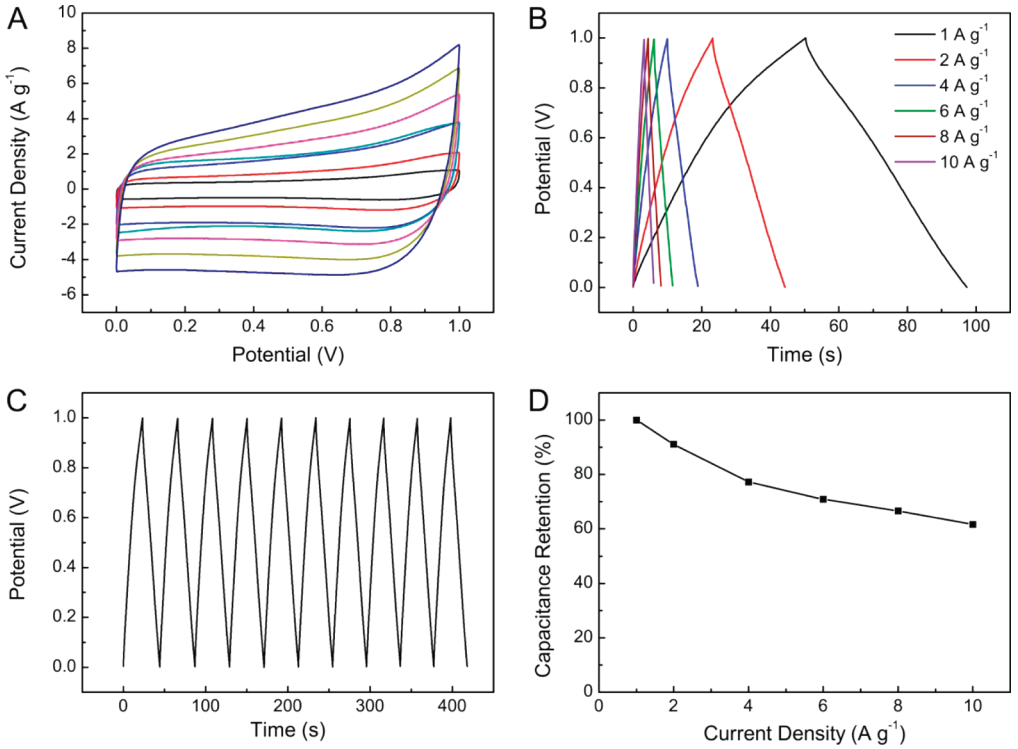

Figure 6. Electrochemical performance of the symmetric supercapacitor of MnO_2-NF//MnO_2-NF. (A) Cyclic voltammograms at different scan rates of 10, 20, 40, 60, 80, and 100 mV s^{-1} (from inner to outer). (B) Galvanostatic charge/discharge curves at different current densities of 1, 2, 4, 6, 8, and 10 A g^{-1}. (C) Galvanostatic charge/discharge curves at a constant current density of 2 A g^{-1}. (D) Capacitance retention ratio as a function of discharge currents.

galvanostatic charge/discharge curves of the supercapacitor are linear and symmetric in the total range of potential (Figure 3B). From the slope of galvanostatic charge/discharge curves, the specific capacitance (C_{sc}) of GH is calculated to be 157.7 F g^{-1} at a current density of 1 A g^{-1}. When the current density increases to 10 A g^{-1}, the specific capacitance is 92.0 F g^{-1}, maintaining 58.3% of that at the current density of 1 A g^{-1} (Figure 3C). The high-rate capability is possibly due to the 3D porous structure and improved conductivity of the L-glutathione reduced GH. The aggregated RGO was mixed with carbon black as the conducting agent and PVDF as the binder in a mass ratio of 8:1:1 to fabricate a symmetric supercapacitor of RGO//RGO. The aggregation of graphene nanosheets lead to reduced active sites for electrolyte ions, and consequently, in comparison with GH, RGO exhibits a much lower specific capacitance of 114.5 F g^{-1} at a current density of 1 A g^{-1} (Figure 3D).

3.2. Positive Electrode Materials. Nickel foam, with excellent electrical conductivity, is featured of cross-linked grids, providing higher porosity and surface area than conventional metal plates (Figure 4A,B).[52,53] After electrodeposition in aqueous solution of manganese acetate at −1.6 V, the smooth surface of the nickel foam skeleton (Figure 4C) became decorated with a dark brown thin film of MnO_2 (Figure 4A). The deposited MnO_2 with nanoplate structure is uniformly coated on the grid of nickel foam and builds up an interconnected network with highly porous structures (Figure 4D,E,F). The formation of nanoplate structure is probably due to the generation of H_2 bubbles at the negative enough potential (−1.6 V), which function as dynamic templates for the electrodeposition.[54,55] Importantly, the hierarchical structure of MnO_2-NF is beneficial for improved electrochemical performance of the active materials, because it would lead to fast ion/electron transfer and sufficient contact between active materials and electrolytes. The unique network structure constituted of vertically aligned MnO_2 nanoplates can also provide necessary free spaces between the individual nanostructures to relax the volume change during continuous charge/discharge reactions.

EDS measurement confirms the presence of the elements of manganese and oxygen in the deposited materials, whereas no other chemical elements, such as sodium and sulfur present in the salt precursors, were detectable (Figure 5A). XPS was conducted for a better understanding of the chemical composition of the cathodic-deposited material. The Mn $2p_{3/2}$ peak is at 641.9 eV, and the Mn $2p_{1/2}$ peak centers at 653.4 eV, with a spin-energy separation of 11.5 eV (Figure 5B). These results are in accordance with the reported data of Mn $2p_{3/2}$ and Mn $2p_{1/2}$ in MnO_2.[56] The XRD pattern of MnO_2-NF exhibits the diffraction peaks from nickel substrate and several broad peaks with low intensity, which can be assigned to ε-MnO_2 (Figure 5C).[57] The formation of MnO_2 is probably the result of a sequential process that involves electrolysis of water and electrochemical reduction of O_2 which leads to increased local pH, precipitation of $Mn(OH)_2$, and finally oxidation of $Mn(OH)_2$ in air to form MnO_2.[58]

MnO_2-NF can also be directly used to fabricate supercapacitors by eliminating the need of polymer binders and conducting additives. The specific capacitance was found to be dependent on the amount and morphology of MnO_2 on nickel foam. With the electrodeposition time increasing from 50 to 200 s, MnO_2 with multilayered structures evolved from monolayer nanoplates (Figure S5, Supporting Information), the weight of MnO_2 increased from 0.6 to 1.7 mg, and its

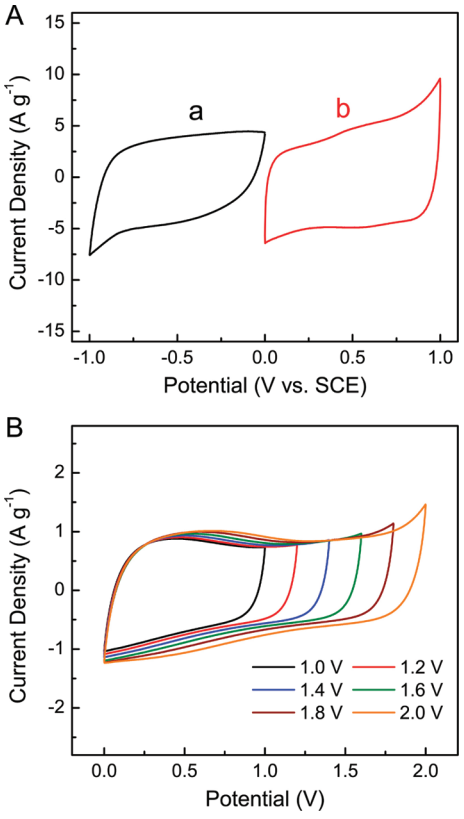

Figure 7. (A) Comparative cyclic voltammograms of GH (a) and MnO_2-NF (b) electrodes in a three-electrode system at a scan rate of 20 mV s^{-1}. (B) Cyclic voltammograms of the asymmetric supercapacitor of GH//MnO_2-NF measured at different potential windows at a scan rate of 20 mV s^{-1}.

specific capacitance (C_{sc}) decreased from 266.8 to 110.8 F g^{-1} at the current density of 1 A g^{-1} (Figure S6, Supporting Information). The formation of thick nanoplates could reduce the specific surface area of MnO_2 exposed to electrolyte ions and result in the decrease of the specific capacitance. Taking into account the mass and specific capacitance of MnO_2, the electrodeposition time was fixed at 100 s for further investigations. The specific capacitance of MnO_2 deposited for 100 s is 194.6 F g^{-1} at the current density of 1 A g^{-1}. The obtained MnO_2 nanoplates exhibit a large BET specific surface area of 59.0 m^2 g^{-1} with a pore size distribution in the range of 2−10 nm (Figure S7, Supporting Information). Figure 6A shows the CV and galvanostatic charge/discharge curves of the symmetric supercapacitor of MnO_2-NF//MnO_2-NF in aqueous Na_2SO_4 electrolyte. The typical rectangular shape of all CV curves measured at different scan rates indicates the perfect capacitive behavior of the supercapacitor (Figure 6A). The galvanostatic charge/discharge curves are very symmetrical in the total range of potential, and the slope of every curve is potential independent with a constant value at a specified current density (Figure 6B,C). Resulting from the unique hierarchical structure of MnO_2-NF and the robust contact between MnO_2 nanoplates and nickel foam endowed by the electrodeposition method, the supercapacitor possesses superior rate capability. When the current density increased to 10 A g^{-1}, the specific capacitance still reached 120.0 F g^{-1}, about 62% of that at 1 A g^{-1} (Figure 6D).

3.3. Asymmetric Hybrid Supercapacitor. An asymmetric supercapacitor was fabricated using MnO_2-NF and GH as the positive and negative electrodes, respectively (Scheme 1). Cyclic voltammetry was first used to estimate the electrochemical potential windows of the electrodes in a three-electrode system with Pt foil and saturated calomel electrode (SCE) as the counter and reference electrodes (Figure 7A). The stable potential window is between −1.0 and 0 V for GH and between 0 and 1.0 V for MnO_2-NF. The cell voltage can be expressed as the sum of the potential range of GH and MnO_2-NF, and consequently, it can be extended up to 2.0 V in 0.5 M aqueous Na_2SO_4 solution for the asymmetric supercapacitor of GH//MnO_2-NF.[59,60] To obtain a 2.0 V operating potential window, it is necessary to balance the charges stored at the positive and negative electrodes. The stored charges (q) are related with the specific capacitance (C_{sc}), the potential window (ΔV), and the mass (m) of the electrode according to $q = C_{sc} \times \Delta V \times m$.[61] Therefore, on the basis of the specific capacitance values and the potential windows of the two materials, the mass ratio between GH and MnO_2 of $m(GH)/m(MnO_2)$ = 1.2 was selected in the asymmetric supercapacitor cell, and indeed, the fabricated asymmetric supercapacitor of GH//MnO_2-NF exhibits a stable potential window up to 2.0 V (Figure 7B). Because the energy density is proportional to the square of the potential, the enlarged potential window gives rise to a remarkably enhanced energy density of supercapacitors. Accordingly, the potential window of 0−2.0 V was chosen for further investigation of the overall electrochemical performance of the asymmetric supercapacitor.

The asymmetric supercapacitor shows relatively rectangular CV curves at scan rates up to 100 mV s^{-1}, indicating a nearly ideal supercapacitor behavior and a desirable fast charge/discharge property (Figure 8A). Galvanostatic charge/discharge tests were also performed with different current densities in a potential window of 0−2.0 V (Figure 8B). The symmetric charge/discharge curves and the linear potential-time profile in the whole potential range also demonstrate a good capacitive behavior with a rapid $I-V$ response of our asymmetric supercapacitor. From the slope of the discharge curve, the specific capacitance (C_t) of the asymmetric supercapacitor is calculated to be 41.7 F g^{-1} based on the total mass of active materials in the two electrodes at a current density of 1 A g^{-1} and still reaches 26.8 F g^{-1} at a high current density of 10 A g^{-1} (Figure 8C). Ragone plots, depicting the relationship of power densities (P) and energy densities (E), were further used to evaluate the performance of the three types of supercapacitors (Figure 8D). The energy density of the asymmetric supercapacitor of GH//MnO_2-NF with a cell voltage of 2.0 V is much higher than that of the symmetric supercapacitors of MnO_2-NF//MnO_2-NF and GH//GH with a cell voltage of 1.0 V at the same power density. Specifically, compared with the symmetric supercapacitors of MnO_2-NF//MnO_2-NF (6.7 Wh kg^{-1}) and GH//GH (5.5 Wh kg^{-1}), an about 3-fold increase of energy density is obtained for the asymmetric supercapacitor of GH//MnO_2-NF (23.2 Wh kg^{-1}) at a current density of 1 A g^{-1}. More importantly, the asymmetric supercapacitor can provide a high energy density without sacrificing power density. When the power density increases to 10.0 kW kg^{-1}, the energy density of GH//MnO_2-NF still reaches 14.9 Wh kg^{-1} at current density of 10 A g^{-1}. The maximum energy density obtained for the asymmetric supercapacitor of GH//MnO_2-NF at a current density of 1 A g^{-1} is comparable or higher than those of MnO_2-based asymmetric supercapacitors with aqueous electrolyte solutions, such as PEDOT//MnO_2 (13.5 Wh kg^{-1}, at a current density of 0.25 A g^{-1}),[62] FeOOH//MnO_2 (24 Wh kg^{-1}, at a

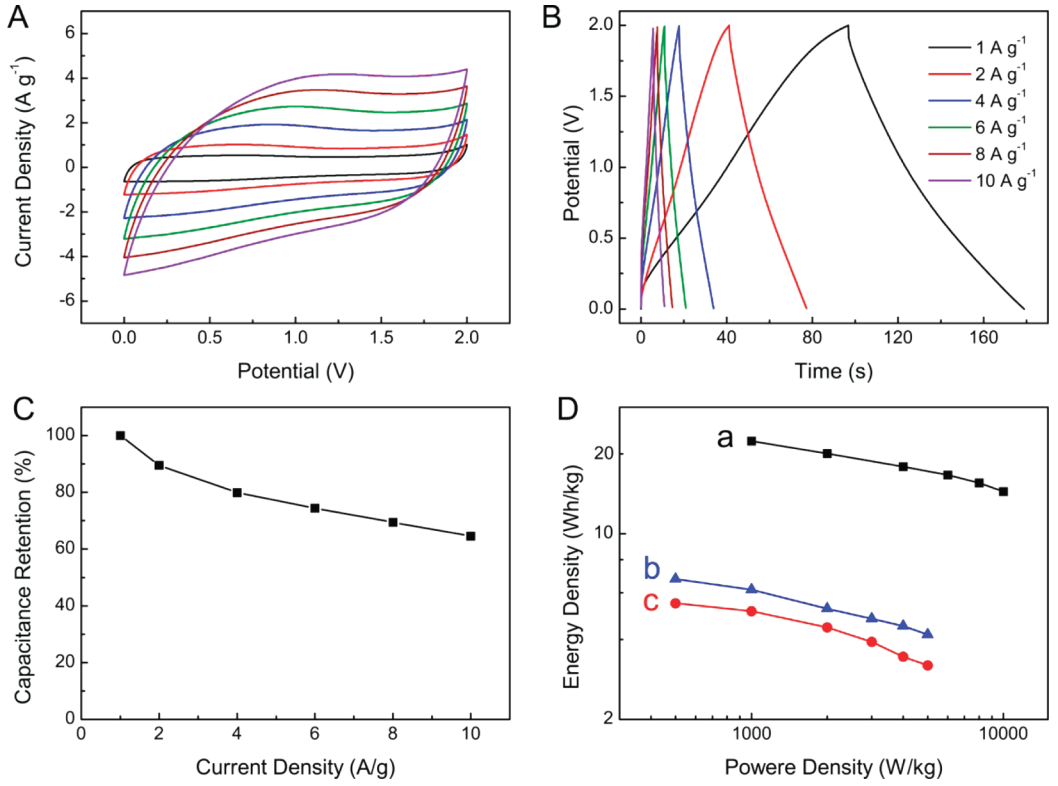

Figure 8. Electrochemical performance of the asymmetric supercapacitor of GH//MnO_2-NF. (A) Cyclic voltammograms at different scan rates of 10, 20, 40, 60, 80, and 100 mV s^{-1} (from inner to outer). (B) Galvanostatic charge/discharge curves at different current densities of 1, 2, 4, 6, 8, and 10 A g^{-1}. (C) Capacitance retention ratio as a function of discharge currents. (D) Ragone plots of the asymmetric supercapacitor of GH//MnO_2-NF (a) and symmetric supercapacitors of MnO_2-NF//MnO_2-NF (b) and GH//GH (c).

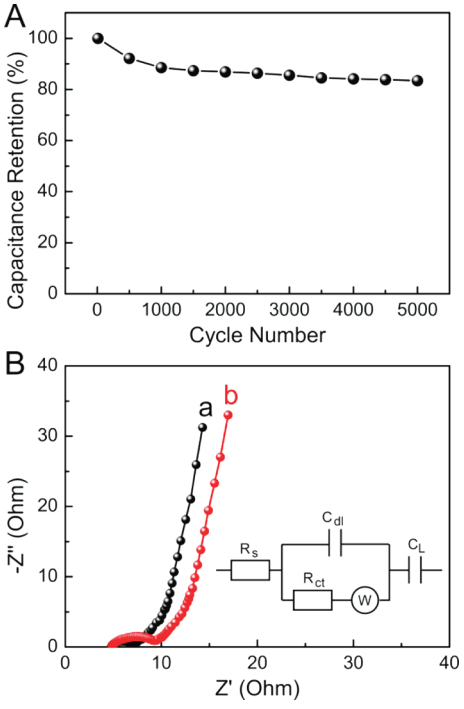

Figure 9. Cycle performance of the asymmetric supercapacitor of GH//MnO_2-NF. (A) Capacitance retention ratio as a function of cycle numbers. (B) Nyquist plots in the frequency range of 0.1 Hz to 10 kHz before (a) and after (b) 5000 cycles, and the electrical equivalent circuit used for fitting impedance spectra.

current density of 0.5 A g^{-1}),[63] activated carbon//MnO_2 (17.3 Wh kg^{-1}, at a current density of 0.55 A g^{-1}),[64] activated carbon//$NaMnO_2$ (19.5 Wh kg^{-1}, at a current density of ~0.04 A g^{-1}),[65] activated carbon//mesoporous MnO_2 (10.4 Wh kg^{-1}, at a current density of ~0.3 A g^{-1}),[66] and activated carbon// $K_{0.27}MnO_2{\cdot}0.6H_2O$ (25.3 Wh kg^{-1}, at a current density of ~0.06 A g^{-1}).[67]

In addition, our asymmetric supercapacitor exhibited excellent cycling stability, which is one of the most important requirements in practical applications. The cycling test of our device shows capacitance retention of 83.4% over 5000 cycles (Figure 9A). Although occasional cracks were observed in MnO_2-NF electrode after the cycling test, MnO_2 was still uniformly coated on the branches of nickel foam and maintained its nanoplate structure (Figure S8, Supporting Information). Electrochemical impedance spectroscopy (EIS) was used to investigate the resistance change of the asymmetric supercapacitor before and after the cycle tests. Nyquist plots were analyzed by the software of ZSimpWin on the basis of the equivalent circuit (Figure 9B). In the low-frequency region, the impedance plot increases sharply and tends to become vertical lines, which are the characteristics of pure capacitive behavior. At the high frequencies, the intercept at real axis (Z') represents the combined resistance (R_s) including ionic resistance of electrolyte, intrinsic resistance of substrate, and contact resistance at the interface of active material/current collector. The semicircle represents the charge transfer resistance (R_{ct}) at the electrode/electrolyte interface.[68] After 5000 cycles, nearly no change was observed for R_s (4.9 Ω), and only a slight increase of R_{ct} from 2.0 to 3.7 Ω was observed. These EIS

results further demonstrate the exceptional stability of the asymmetric supercapacitor.

4. CONCLUSIONS

GH with 3D interconnected pores was successfully prepared by reducing GO with an eco-friendly reagent of L-glutathione under mild conditions. Vertically aligned MnO_2 nanoplates were uniformly deposited on porous nickel foam under cathodic conditions. Asymmetric supercapacitor was fabricated using these two materials as negative and positive electrodes, respectively. Benefitting from 3D GH with well-preserved graphene nanosheets, vertically aligned MnO_2 nanoplates with sufficient free spaces, and the robust contact between MnO_2 and nickel foam, the asymmetric supercapacitor of GH//MnO_2-NF exhibits stable cycling performance and remarkable energy density of 23.2 Wh kg^{-1}. Such asymmetric supercapacitor offers great promise in the application of high-performance energy storage systems because of its advantages of low-cost, facile fabrication process, high energy and power density, and eco-friendly nature.

■ ASSOCIATED CONTENT

Ⓢ Supporting Information

Supplementary figures. This material is available free of charge via the Internet at http://pubs.acs.org.

■ AUTHOR INFORMATION

Corresponding Author

*E-mail: hduan@ntu.edu.sg.

Notes

The authors declare no competing financial interest.

■ ACKNOWLEDGMENTS

H.D. thanks the program of Nanyang Assistant Professorship for financial support. H.G. is a recipient of graduate research scholarship supported by Nanyang Technological University, Singapore.

■ REFERENCES

(1) Hall, P. J.; Mirzaeian, M.; Fletcher, S. I.; Sillars, F. B.; Rennie, A. J. R.; Shitta-Bey, G. O.; Wilson, G.; Cruden, A.; Carter, R. *Energy Environ. Sci.* **2010**, *3*, 1238−1251.
(2) Simon, P.; Gogotsi, Y. *Nat. Mater.* **2008**, *7*, 845−854.
(3) Kotz, R.; Carlen, M. *Electrochim. Acta* **2000**, *45*, 2483−2498.
(4) Frackowiak, E. *Phys. Chem. Chem. Phys.* **2007**, *9*, 1774−1785.
(5) Lee, S. W.; Gallant, B. M.; Byon, H. R.; Hammond, P. T.; Shao-Horn, Y. *Energy Environ. Sci.* **2011**, *4*, 1972−1985.
(6) Zhang, L. L.; Zhou, R.; Zhao, X. S. *J. Mater. Chem.* **2010**, *20*, 5983−5992.
(7) Du, F.; Yu, D. S.; Dai, L. M.; Ganguli, S.; Varshney, V.; Roy, A. K. *Chem. Mater.* **2011**, *23*, 4810−4816.
(8) Sun, Y. Q.; Wu, Q.; Shi, G. Q. *Phys. Chem. Chem. Phys.* **2011**, *13*, 17249−17254.
(9) Stoller, M. D.; Park, S. J.; Zhu, Y. W.; An, J. H.; Ruoff, R. S. *Nano Lett.* **2008**, *8*, 3498−3502.
(10) Chen, Y.; Zhang, X. O.; Zhang, D. C.; Yu, P.; Ma, Y. W. *Carbon* **2011**, *49*, 573−580.
(11) Vivekchand, S. R. C.; Rout, C. S.; Subrahmanyam, K. S.; Govindaraj, A.; Rao, C. N. R. *J. Chem. Sci.* **2008**, *120*, 9−13.
(12) Wang, Y. G.; Xia, Y. Y. *Electrochem. Commun.* **2005**, *7*, 1138−1142.
(13) Zhao, X.; Sanchez, B. M.; Dobson, P. J.; Grant, P. S. *Nanoscale* **2011**, *3*, 839−855.
(14) Demarconnay, L.; Raymundo-Pinero, E.; Beguin, F. *J. Power Sources* **2011**, *196*, 580−586.
(15) Conway, B. E.; Pell, W. G. *J. Solid State Electrochem.* **2003**, *7*, 637−644.
(16) Pell, W. G.; Conway, B. E. *J. Power Sources* **2004**, *136*, 334−345.
(17) Long, J. W.; Belanger, D.; Brousse, T.; Sugimoto, W.; Sassin, M. B.; Crosnier, O. *MRS Bull.* **2011**, *36*, 513−522.
(18) Wang, G. P.; Zhang, L.; Zhang, J. J. *Chem. Soc. Rev.* **2012**, *41*, 797−828.
(19) Chen, P. C.; Shen, G. Z.; Shi, Y.; Chen, H. T.; Zhou, C. W. *ACS Nano* **2010**, *4*, 4403−4411.
(20) Zhang, J. T.; Jiang, J. W.; Li, H. L.; Zhao, X. S. *Energy Environ. Sci* **2011**, *4*, 4009−4015.
(21) Yu, G. H.; Hu, L. B.; Vosgueritchian, M.; Wang, H. L.; Xie, X.; McDonough, J. R.; Cui, X.; Cui, Y.; Bao, Z. N. *Nano Lett.* **2011**, *11*, 2905−2911.
(22) Brousse, T.; Toupin, M.; Belanger, D. *J. Electrochem. Soc.* **2004**, *151*, A614−A622.
(23) Jiang, H.; Li, C. Z.; Sun, T.; Ma, J. *Nanoscale* **2012**, *4*, 807−812.
(24) Wang, Y.; Shi, Z. Q.; Huang, Y.; Ma, Y. F.; Wang, C. Y.; Chen, M. M.; Chen, Y. S. *J. Phys. Chem. C* **2009**, *113*, 13103−13107.
(25) Mishra, A. K.; Ramaprabhu, S. *J. Phys. Chem. C* **2011**, *115*, 14006−14013.
(26) Xu, Y. X.; Sheng, K. X.; Li, C.; Shi, G. Q. *ACS Nano* **2010**, *4*, 4324−4330.
(27) Sheng, K. X.; Xu, Y. X.; Li, C.; Shi, G. Q. *New Carbon Mater.* **2011**, *26*, 9−15.
(28) Qu, Q. T.; Zhang, P.; Wang, B.; Chen, Y. H.; Tian, S.; Wu, Y. P.; Holze, R. *J. Phys. Chem. C* **2009**, *113*, 14020−14027.
(29) Hu, L. B.; Chen, W.; Xie, X.; Liu, N. A.; Yang, Y.; Wu, H.; Yao, Y.; Pasta, M.; Alshareef, H. N.; Cui, Y. *ACS Nano* **2011**, *5*, 8904−8913.
(30) Ghodbane, O.; Pascal, J. L.; Favier, F. *ACS Appl. Mater. Interfaces* **2009**, *1*, 1130−1139.
(31) Chou, S. L.; Wang, J. Z.; Chew, S. Y.; Liu, H. K.; Dou, S. X. *Electrochem. Commun.* **2008**, *10*, 1724−1727.
(32) Wei, W. F.; Cui, X. W.; Chen, W. X.; Ivey, D. G. *Chem. Soc. Rev.* **2011**, *40*, 1697−1721.
(33) Wu, M. S.; Chiang, P. C. J. *Electrochem. Solid State Lett.* **2004**, *7*, A123−A126.
(34) Wei, W. F.; Cui, X. W.; Mao, X. H.; Chen, W. X.; Ivey, D. G. *Electrochim. Acta* **2011**, *56*, 1619−1628.
(35) Zhao, D. D.; Yang, Z.; Zhang, L. Y.; Feng, X. L.; Zhang, Y. F. *Electrochem. Solid State Lett.* **2011**, *14*, A93−A96.
(36) Wang, Y. H.; Zhitomirsky, I. *Mater. Lett.* **2011**, *65*, 1759−1761.
(37) Hummers, W. S.; Offeman, R. E. *J. Am. Chem. Soc.* **1958**, *80*, 1339−1339.
(38) Gao, H. C.; Xiao, F.; Ching, C. B.; Duan, H. W. *ACS Appl. Mater. Interfaces* **2011**, *3*, 3049−3057.
(39) Liu, D. W.; Zhang, Q. F.; Xiao, P.; Garcia, B. B.; Guo, Q.; Champion, R.; Cao, G. Z. *Chem. Mater.* **2008**, *20*, 1376−1380.
(40) Stoller, M. D.; Ruoff, R. S. *Energy Environ. Sci.* **2010**, *3*, 1294−1301.
(41) Zhang, L.; Shi, G. Q. *J. Phys. Chem. C* **2011**, *115*, 17206−17212.
(42) Pham, T. A.; Kim, J. S.; Kim, J. S.; Jeong, Y. T. *Colloid Surf., A: Physicochem. Eng. Aspects* **2011**, *384*, 543−548.
(43) Chen, W. F.; Yan, L. F. *Nanoscale* **2011**, *3*, 3132−3137.
(44) Bai, H.; Li, C.; Wang, X. L.; Shi, G. Q. *J. Phys. Chem. C* **2011**, *115*, 5545−5551.
(45) Zhang, X. T.; Sui, Z. Y.; Xu, B.; Yue, S. F.; Luo, Y. J.; Zhan, W. C.; Liu, B. *J. Mater. Chem.* **2011**, *21*, 6494−6497.
(46) Gao, J.; Liu, F.; Liu, Y. L.; Ma, N.; Wang, Z. Q.; Zhang, X. *Chem. Mater.* **2010**, *22*, 2213−2218.
(47) Chen, D. Z.; Li, L. D.; Guo, L. *Nanotechnology* **2011**, *22*, 325601.
(48) Kulakov, V. A.; Shishlyannikova, N. Y.; Virnik, A. D. *J. Appl. Spectrosc.* **1987**, *46*, 619−625.
(49) Fan, Z. J.; Wang, K.; Wei, T.; Yan, J.; Song, L. P.; Shao, B. *Carbon* **2010**, *48*, 1686−1689.

(50) Moon, I. K.; Lee, J.; Ruoff, R. S.; Lee, H. *Nat. Commun.* **2010**, *1*, 73.
(51) Pei, S. F.; Zhao, J. P.; Du, J. H.; Ren, W. C.; Cheng, H. M. *Carbon* **2010**, *48*, 4466−4474.
(52) Xue, L. G.; Hao, H.; Wei, Z.; Huang, T.; Yu, A. S. *J. Solid State Electrochem.* **2011**, *15*, 485−491.
(53) Wang, Y. L.; Zhao, Y. Q.; Xu, C. L. *J. Solid State Electrochem.* **2012**, *16*, 829−834.
(54) Xiao, W.; Xia, H.; Fuh, J. Y. H.; Lu, L. *J. Electrochem. Soc.* **2009**, *156*, A627−A633.
(55) Liu, D. W.; Garcia, B. B.; Zhang, Q. F.; Guo, Q.; Zhang, Y. H.; Sepehri, S.; Cao, G. Z. *Adv. Funct. Mater.* **2009**, *19*, 1015−1023.
(56) Lu, X. H.; Zheng, D. Z.; Zhai, T.; Liu, Z. Q.; Huang, Y. Y.; Xie, S. L.; Tong, Y. X. *Energy Environ. Sci.* **2011**, *4*, 2915−2921.
(57) Kim, C. H.; Akase, Z.; Zhang, L. C.; Heuer, A. H.; Newman, A. E.; Hughes, P. J. *J. Solid State Chem.* **2006**, *179*, 753−774.
(58) Zhu, C. Z.; Guo, S. J.; Fang, Y. X.; Han, L.; Wang, E. K.; Dong, S. J. *Nano Res.* **2011**, *4*, 648−657.
(59) Brousse, T.; Taberna, P. L.; Crosnier, O.; Dugas, R.; Guillemet, P.; Scudeller, Y.; Zhou, Y.; Favier, F.; Belanger, D.; Simon, P. *J. Power Sources* **2007**, *173*, 633−641.
(60) Khomenko, V.; Raymundo-Pinero, E.; Beguin, F. *J. Power Sources* **2006**, *153*, 183−190.
(61) Fan, Z. J.; Yan, J.; Wei, T.; Zhi, L. J.; Ning, G. Q.; Li, T. Y.; Wei, F. *Adv. Funct. Mater.* **2011**, *21*, 2366−2375.
(62) Khomenko, V.; Raymundo-Pinero, E.; Frackowiak, E.; Beguin, F. *Appl. Phys. A: Mater. Sci. Process.* **2006**, *82*, 567−573.
(63) Jin, W. H.; Cao, G. T.; Sun, J. Y. *J. Power Sources* **2008**, *175*, 686−691.
(64) Cottineau, T.; Toupin, M.; Delahaye, T.; Brousse, T.; Belanger, D. *Appl. Phys. A: Mater. Sci. Process.* **2006**, *82*, 599−606.
(65) Qu, Q. T.; Shi, Y.; Tian, S.; Chen, Y. H.; Wu, Y. P.; Holze, R. *J. Power Sources* **2009**, *194*, 1222−1225.
(66) Wang, Y. T.; Lu, A. H.; Zhang, H. L.; Li, W. C. *J. Phys. Chem. C* **2011**, *115*, 5413−5421.
(67) Qu, Q. T.; Li, L.; Tian, S.; Guo, W. L.; Wu, Y. P.; Holze, R. *J. Power Sources* **2010**, *195*, 2789−2794.
(68) Fic, K.; Lota, G.; Meller, M.; Frackowiak, E. *Energy Environ. Sci.* **2012**, *5*, 5842−5850.